Signal Processing: *Image Communication* 40 (2016) 1–15

Contents lists available at ScienceDirect

Signal Processing: *Image Communication*

journal homepage: www.elsevier.com/locate/image

Blind image quality assessment by relative gradient statistics and adaboosting neural network ☆

Lixiong Liu [a], Yi Hua [a], Qingjie Zhao [a], Hua Huang [a,*], Alan Conrad Bovik [b]

[a] *Beijing Laboratory of Intelligent Information Technology, School of Computer Science and Technology, Beijing Institute of Technology, Beijing 100081, China*

[b] *Laboratory for Image and Video Engineering, Department of Electrical and Computer Engineering, The University of Texas at Austin, Austin, TX 78712, USA*

ARTICLE INFO

Article history:
Received 9 May 2015
Received in revised form
24 October 2015
Accepted 24 October 2015
Available online 2 November 2015

Keywords:
No reference (NR)
Image quality assessment (IQA)
Spatial correlation
Oriented gradient correlation
AdaBoosting neural network

ABSTRACT

The image gradient is a commonly computed image feature and a potentially predictive factor for image quality assessment (IQA). Indeed, it has been successfully used for both full- and no- reference image quality prediction. However, the gradient orientation has not been deeply explored as a predictive source of information for image quality assessment. Here we seek to amend this by studying the quality relevance of the relative gradient orientation, viz., the gradient orientation relative to the surround. We also deploy a relative gradient magnitude feature which accounts for perceptual masking and utilize an AdaBoosting back-propagation (BP) neural network to map the image features to image quality. The generalization of the AdaBoosting BP neural network results in an effective and robust quality prediction model. The new model, called Oriented Gradients Image Quality Assessment (OG-IQA), is shown to deliver highly competitive image quality prediction performance as compared with the most popular IQA approaches. Furthermore, we show that OG-IQA has good database independence properties and a low complexity.

1. Introduction

Given the exploding development and deployment of visual acquisition, display and processing technologies, digital images have become ubiquitous in our daily life. Advanced image capture devices that are built into digital cameras, smart phones and wearable devices now allow us to acquire high resolution images frequently and conveniently. Users can easy and nearly instantly share and receive these images conveniently via social websites such as Facebook and Flickr. These images often suffer from quality degradations caused by distortion, hence image quality assessment (IQA) models that can accurately predict human subjective judgments remain an important topic of research. Subjective assessment of image quality is time-consuming and difficult to exploit. So the development of objective IQA models, especially blind or no-reference (NR) models that operate without reference image data, are of particular relevance. A successful IQA model can be applied to improve many image processing applications including image acquisition, processing and transmission [1]. For example, an NR IQA model can be used to monitor image communication channels, and in particular can be used to predict image quality to provide feedback to optimize image transmission.

Generally speaking, objective IQA models can be categorized into full-reference (FR) approaches [2–14], reduced-reference (RR) approaches such as [15], and NR approaches [16–36]. FR and RR approaches need all or part

☆ This work is supported in part by the National Natural Science Foundation of China under Grant 61133008.

* Corresponding author.
E-mail addresses: lxliu@bit.edu.cn (L. Liu), hatcat@bit.edu.cn (Y. Hua), zhaoqj@bit.edu.cn (Q. Zhao), huahuang@bit.edu.cn (H. Huang), bovik@ece.utexas.edu (A.C. Bovik).

http://dx.doi.org/10.1016/j.image.2015.10.005
0923-5965/

of the original image information to form quality prediction while NR approaches operate entirely absent any reference image. Under circumstances where original images are not available, as in most mobile and photographic situations, NR approaches offer the greatest freedom and flexibility, and recently have attracted intensive research.

Many effective FR IQA approaches utilize the image gradient (such as FSIM [4], ESSIM [5], GMSD [6] and VGS [8]), however not all aspects of the gradient have been deeply explored for IQA, in particular, the gradient orientation [8]. The majority of successful NR IQA approaches utilize models of natural image statistics to detect differences between natural high-quality images and distorted ones (e.g., the generalized gaussian and gaussian scale mixture models of image wavelet coefficients used by DIIVINE [16], of DCT coefficients in BLIINDS [17], of curvelet coefficients in CurveletQA [27] and related models of the smoothed image gradient magnitude and laplacian used by BIQA [28]). The image gradient orientation and its relevance for visual quality prediction remains an interesting avenue of research.

Natural images are highly structured and correlated over orientations and scales [37]. Local statistics based orientation models are used in BRISQUE [19] to conduct image quality assessment, while the Histograms of Oriented Gradients (HOG) [38] method has been successfully used to develop a variety of modes of human detection. Local orientation dependencies of bandpass or gradient images contain significant information regarding image naturalness and object structure [6,19,28,39]. This information is modified by the introduction of image distortion. Thus, a promising simple way of approaching the IQA problem is to analyze the correlation structure of image gradient orientations. In this direction, we propose an efficient general-purpose NR IQA model called the Oriented Gradients Image Quality Assessment (OG-IQA) index. This new model further explores the potential of the image gradient for NR IQA beyond the gradient magnitude [6,28]. Thus, our work here complements prior work by using the image gradient orientation, rather than the gradient magnitude, for NR IQA.

Furthermore, an AdaBoosting BP neural network is considered as the learning image quality evaluation model in OG-IQA method. Given its outstanding generalization ability, the classical back-propagation (BP) neural network has been widely used for classification and regression. The performance of the network can be further improved by simple ensemble realization [40]. One of the most useful ensemble methods is adaptive boosting (viz., AdaBoost) [41,42] which delivers impressive performance. It has been amply demonstrated that a boosting ensemble generally outperforms a single network, and may produce large gains in accuracy [43]. The AdaBoost algorithm is based on combining many relatively Weak Learners to build a stronger regression machine [44]. Here, we deploy the AdaBoosting BP neural network to conduct quality prediction on distorted images across multiple distortion categories, using quality-predictive oriented image gradient features. The LIVE image database [45,46] is used for performance evaluation of the model. The experimental results indicate that OG-IQA correlates exceptionally well with human subject judgments of image quality.

The rest of the paper is organized as follows. Section 2 reviews previous work on NR IQA. Section 3 and Section 4 describe limitations of off-the-shelf IQA algorithms and gradient magnitude based feature extraction methods. Section 5 details the feature learning method, an AdaBoosting BP neural network. Section 6 presents experimental results. Finally, we conclude the paper in Section 7.

2. Related work

2.1. General-purpose NR IQA models

NR IQA models generally involve two steps: feature extraction and feature learning based quality assessment. The performances of these methods rely on both the perceptual relevance of the extracted features and on the method of feature learning. Natural scene statistics (NSS) models, such as the Gaussian Scale Mixture (GSM) model have been shown to be both perceptually relevant and highly regular descriptors of natural images [37,47]. Recently Gao et al. proposed a NSS-based IQA model which used multiple kernel function instead of a single RFB function [26]. Hou et al. solved the IQA problem via a novel deep learning algorithm [29]. Narwaria and Lin utilized a support vector regression (SVR) to learn to fuse image features into quality score predictions [30]. Brando and Queluz found that the parameters of a Laplace probability density model of the DCT coefficients of JPEG compressed images correlates well with the severity of blocking effects [21]. Sheikh et al. used the joint histogram of wavelet coefficients to perform NR IQA on JPEG2000 compressed images [22]. Li et al. extracted image features including phase congruency, entropy and gradient magnitude, and used them to train a general regression neural network (GRNN) to solve the NR IQA problem on multiple distortion categories [23]. Saad et al. proposed a new method for NR IQA named BLIINDS [17,24]. BLIINDS transforms the images to the block DCT domain, then utilizes a generalized Gaussian distribution (GGD) model fit to reduce the NSS feature vector dimension. Moorthy et al. proposed a 2-stage framework for NR IQA [16,18] which uses NSS features extracted from a distorted image for distortion identification and subsequent distortion-specific IQA. Mittal et al. contributed a new NSS-based NR IQA method that operates in the spatial domain named BRISQUE [19]. BRISQUE is based on bandpass filtering and local nonlinear divisive normalization to reduce the correlations between the bandpass responses. Mittal et al. further utilized the image features in BRISQUE to develop training-free IQA models [31,48]. Xue et al. proposed an unsupervised algorithm based on natural image statistics theory [32]. Ye et al. proposed unsupervised algorithms based on designed visual codebooks [33,34]. Ke et al. extracted the image features using the human visual system and the free-energy-based brain theory [35]. Ke et al. solved the NR IQA for blur images using a sharpness metric in the autoregressive (AR) parameter space [36]. Overall, research in this area continues to thrive [49]. We can also

observe that the novel learning evaluation models are meaningful to the IQA field. Thus, we utilize an Adaboosting BP neural network as the learning evaluation model in our method.

2.2. Existing gradient-based IQA approaches

The image gradient has been widely used in the IQA field owing to the rich information it conveys regarding image edges and structures. It also exhibits statistical regularities on naturalistic images. For example, Zhang et al. used phase congruency along with the gradient magnitude to compute and weight local quality scores [4]. Zhang et al. utilized anisotropic regularity and irregularity of the image edges to estimate image quality [5]. Xue et al. used the variance of a gradient magnitude similarity map to estimate the image quality [6]. Liu et al. proposed a full-reference algorithm which uses the contrast between pristine and distorted oriented gradient maps to compute image quality [7]. Zhu et al. proposed a FR IQA model combining the image gradient magnitude with comparisons of image gradient magnitude and orientation to predict the quality [8]. Yang et al. combined HOG with the structural similarity (SSIM) index to create a FR IQA index [9]. Cheng et al. proposed a reduced reference image quality assessment model based on NSS and information–theoretic distance measures based on the gradient magnitude [15]. Under the assumption that details revealed by the gradient affect image quality to a large degree, Zhang et al. proposed the Multi-Level Similarity (MLSIM) index for FR IQA [10]. Chen and Bovik use a combination of multiscale gradient and natural image statistic (NSS) features to predict blurred image quality [20]. Xue et al. combine the gradient magnitude with the laplacian of gaussian to form joint statistics which are highly predictive of image quality [28]. Wang el al. compute a Histograms of Oriented Gradients (HOG) based distance measure to evaluate image distortions [12]. Bondzulic et al. utilize the gradient magnitude and gradient orientation to design a new FR image quality metric [13]. The majority of the abovementioned gradient-based algorithms are FR or RR IQA approaches, hence require a pristine reference signal to operate. Here we explore, for the first time, the gradient orientation, expressed as a relative value, as a quality-predictive feature for no-reference IQA.

3. Limitations of gradient-based approaches

Most gradient-based IQA approaches are FR or RR approaches [4–10], while the majority of gradient-based NR approaches are distortion-specific such as [20]. A recent exception is [28], which employs statistics of the gradient magnitude and the laplacian to predict image quality. Based on the success of these approaches, there appear to be strong intrinsic connections between the image gradient and image quality. With a view towards exploring the complementary quality information provided by the image gradient orientation, thereby further deepening our understanding of how to design efficient NR IQA models, we study the relative contributions of the two modes of information. First we explore the estimated image gradient magnitude, defined as:

$$|\nabla I(i,j)| = \sqrt{I_x^2(i,j)+I_y^2(i,j)}, \tag{1}$$

where $I_x(i, j)$ and $I_y(i, j)$ are approximate values of the directional derivatives in the horizontal x and vertical y directions corresponding to sample directions i and j.

3.1. Gradient dislocation vs. gradient distribution

Image distortion clearly exerts a great influence on the image gradient magnitude. However, this effect is largely dominated by shrinkage of the gradient magnitude caused by blur-like distortion processes. However, for other kinds of distortions, changes in the gradient magnitude distributions may be less evident, while still being visually apparent in the image owing to changes in the spatial locations of large gradient magnitude. Using JPEG distortion as an example, the differences between the gradient magnitude maps of a 'pristine' image and a JPEG distorted version of it may be quite visible and numerically significant, even while the histograms of the two gradient magnitude histograms are very similar, making statistical modeling of this quantity less valuable. Fig. 1 depicts an example of this phenomenon.

3.2. Gradient orientation

The scalar-valued gradient magnitude only conveys part of the 'picture' with regards to local image brightness variations. Visual cortical neurons are highly sensitive to local orientation information in images [50,51]. Since image distortions are likely to modify local image anisotropies, it is worth exploring the value of the gradient orientation to augment NR IQA models. For example, both the locations and distributions of the gradient orientation between original image and its JPEG distortion version can be distinguished obviously (see Fig. 2), while the ones of gradient magnitude can cause the problem as shown in Fig. 1.

4. Gradient orientaion features

The gradient orientation conveys information that is complementary to that carried by the gradient magnitude, and has been used to obtain improved FR IQA results. Define the estimated gradient orientation by:

$$\angle\nabla I(i,j) = arc\ \tan\left(\frac{I_y(i,j)}{I_x(i,j)}\right). \tag{2}$$

Orientation is relative, and modern feature extraction mechanisms that utilize gradient orientation information compute it in a relative manner, e.g. SIFT [52] and Histograms of Oriented Gradients (HOG) [53]. Likewise, relative gradient magnitude information can convey much regarding changes in local structure. Image distortions that modify local structure can modify the existing local orientation information. Orientation may be measured absolutely, against the frame of reference of the image coordinate system, or it can be measured in a relative

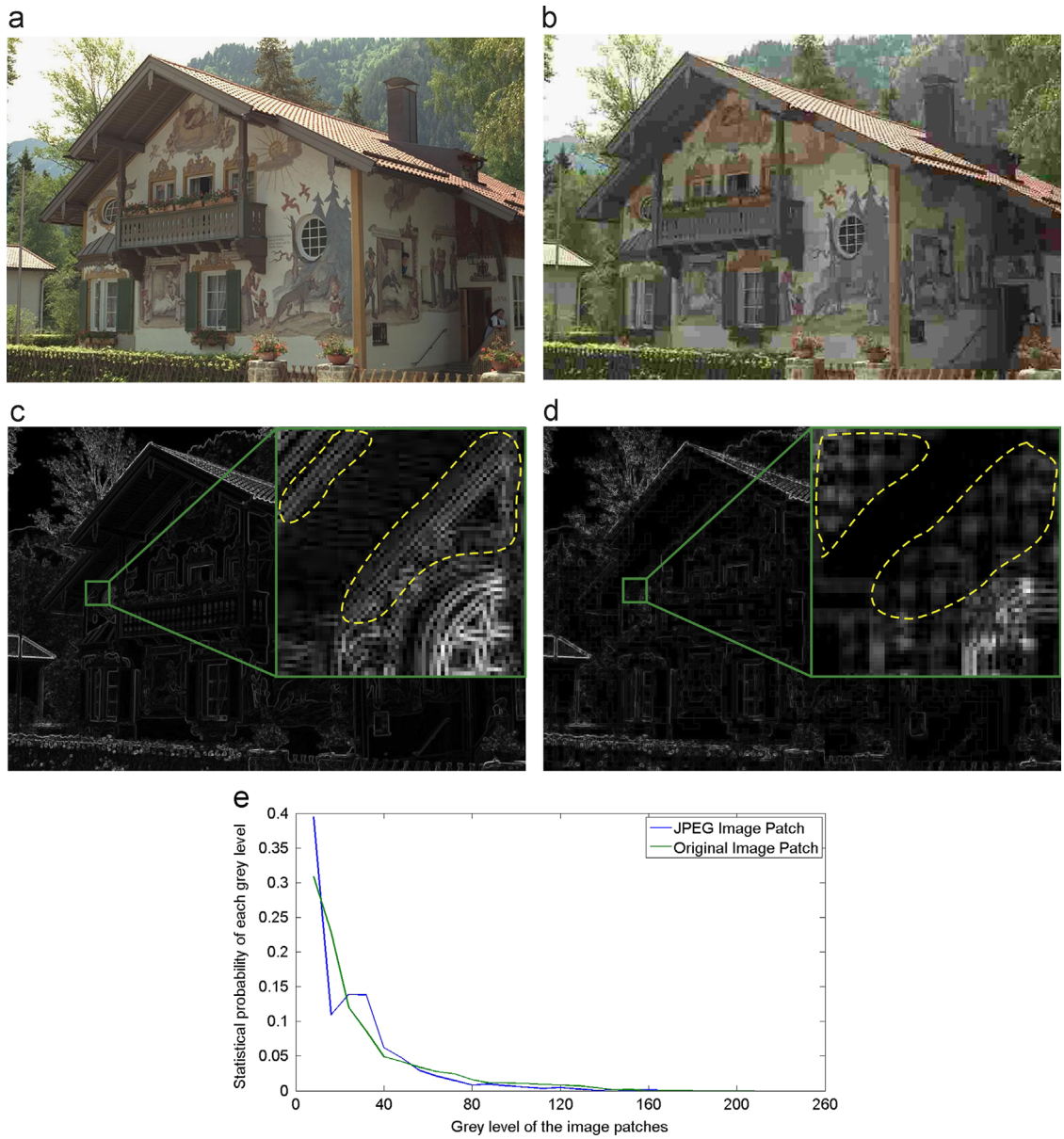

Fig. 1. Differences in the gradient magnitudes of a pristine image and a JPEG distorted version of it. (a) Original image, (b) JPEG distorted image (DMOS = 79.9594 as recorded at the LIVE Database [45]), (c) gradient magnitude of original image, (d) gradient magnitude of JPEG image, (e) histograms of the zoomed image patches in (c) and (d). The yellow lines (manual annotations) in (c) and (d) are roughly aligned with the spatial locations of high gradient magnitude values in the two magnified image patches. The histogram in (e) shows that the locations of high gradient magnitude in the patches are different while having a similar first-order distribution.

manner against the background of local orientations, represented as, for example, an average value. The latter mode of measurement is more relevant for image quality assessment, since relative orientation features can capture departures from the natural distribution of local orientations caused by local degradations of image structure. Following this philosophy, we also define a relative gradient magnitude feature, the similar idea being that impairments to local contrast are best cast against the surrounding contrasts. Indeed, this is a form of the contrast masking principle.

Thus, three types of gradient maps are computed from I_x and I_y, and utilized to characterize the quality-dependent behavior of the image gradient over patches of size $M \times N$: the gradient magnitude (GM), the relative gradient orientation (RO), and the relative gradient magnitude (RM). The GM is given as before by (1) while the RO is given by

$$\angle\nabla I(i,j)_{RO} = \angle\nabla I(i,j) - \angle\nabla I(i,j)_{AVE}, \tag{3}$$

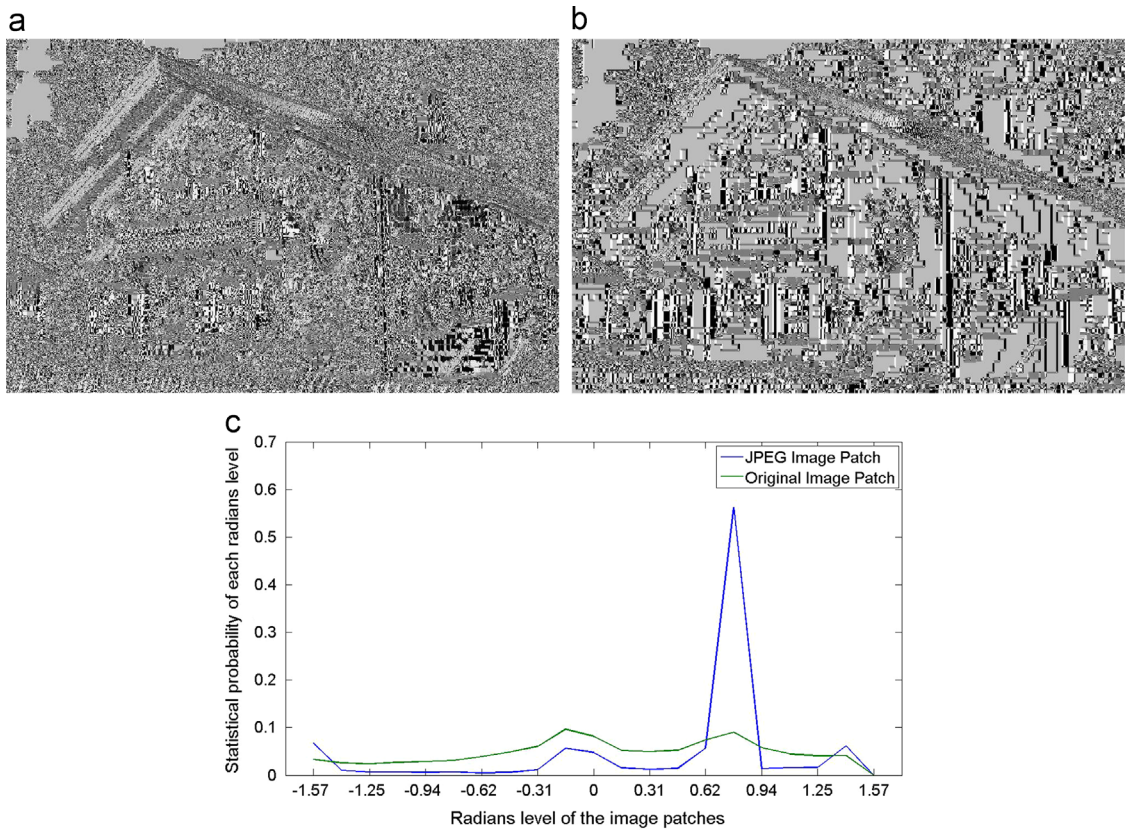

Fig. 2. Differences in the gradient orientations of a pristine image and a JPEG distorted version of it. (a) Gradient orientation of original image in Fig. 1(a), (b) gradient orientation of JPEG image in Fig. 1(b), (c) histograms of the zoomed image patches in Fig. 1(c) and (d). The histogram in (c) shows that the JPEG distortion can obviously degrade gradient orientation by changing most gradient orientation into limited radians (e.g. 0, $\pi/4$ and $\pi/2$).

where the local average orientation is defined to be

$$\angle\nabla I(i,j)_{AVE} = arc\ \tan\left(\frac{I_y(i,j)_{AVE}}{I_x(i,j)_{AVE}}\right),$$

using the average directional derivative estimates

$$I_y(i,j)_{AVE} = \frac{1}{MN}\sum_{(m,n)\in W}\sum I_y(i-m,j-n),$$

and

$$I_x(i,j)_{AVE} = \frac{1}{MN}\sum_{(m,n)\in W}\sum I_x(i-m,j-n),$$

where W is a set of relative coordinate shifts defining the local neighborhood over which the derivative values are taken. For example, if the neighborhood is 3×3 square, then $M=N=3$ and $W=\{(-1,-1),\ (-1,0),\ (-1,1),\ (0,-1),\ (0,0),\ (0,1),\ (1,-1),\ (1,0),\ (1,1)\}$. In fact, our basic implementation uses this neighborhood although we also explore performance against neighborhood size later, in Section 6.

Likewise, the RM is defined as

$$|\nabla I(i,j)|_{RM} = \sqrt{\begin{array}{l}(I_x(i,j)-I_x(i,j)_{AVE})^2\\ \quad +(I_y(i,j)-I_y(i,j)_{AVE})^2\end{array}}, \tag{4}$$

in terms of the average local derivatives.

Cortical neurons are highly sensitive to anisotropic information in images, and image distortion processes can modify and create unnatural local anisotropies [18,22,25]. It is quite possible to create sophisticated, regularized and multiscale estimates of local derivatives, e.g., by Gaussian smoothing, Gaussian pyramid [54], or steerable pyramid [55]. In our implementation, we utilize Gaussian partial derivative aligned filters in the horizontal and vertical directions to compute the values of the directional gradient components, I_x and I_y, respectively. By comparing with other filters (e.g. Sobel and Prewitt), the Gaussian partial derivative aligned filters can be considered as a more smoothed edge filter which is benefit to our following process, such as computing RM and RO. The Gaussian partial derivative filters are given by

$$\nabla_\gamma G(x,y,\sigma) = -\frac{\gamma}{2\pi\sigma^4}\exp\left(-\frac{x^2+y^2}{2\sigma^2}\right), \tag{5}$$

where $G(x,y,\sigma) = -\frac{1}{2\pi\sigma^2}\exp\left(-\frac{x^2+y^2}{2\sigma^2}\right)$ is the Gaussian kernel, and where the Υ represents either the horizontal x or the vertical y direction of partial derivative.

Fig. 3(b)–(d) depicts the three types of gradient and relative gradient characteristics that are considered here, computed on the original picture in Fig. 3(a).

According to our hypothesis, changes to the statistical distributions of the gradient and relative gradient quantities caused by image distortions can be used to quantify

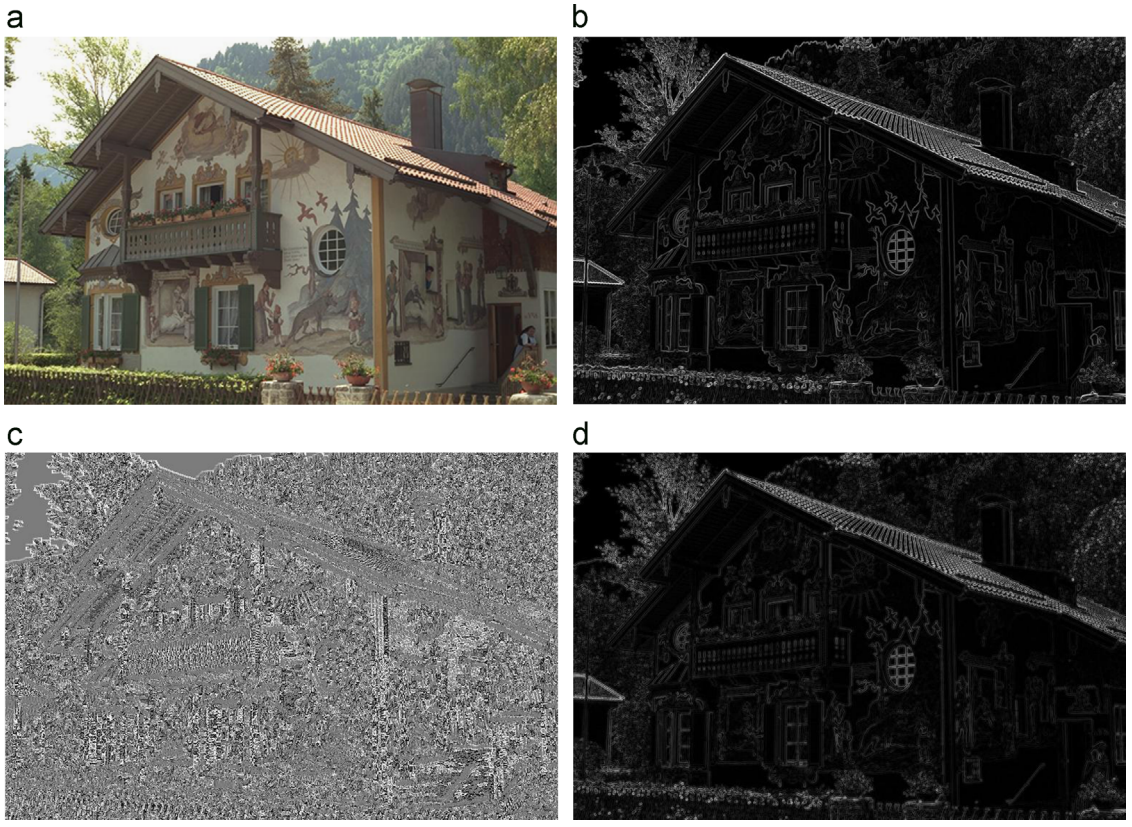

Fig. 3. Gradient and relative gradient maps. (a) Original image, (b) gradient magnitude (GM), (c) relative gradient orientation (RO), (d) relative gradient magnitude (RM).

the degree of perceived image distortion as well as to classify the distortions by type. In the following, we study the behavior of the various gradient characteristic maps on exemplars of the five common distortions contained in the LIVE IQA Database [45,46] (see Figs. 4 and 5). It is apparent that each type of gradient map is deeply and distinctly affected by the five types of distortions.

Fig. 4 depicts GM, RO and RM maps on an exemplar image distorted by each type of LIVE impairment, while Fig. 5 shows the histograms of these same maps on all the same distorted images. Clearly, the histograms are also significantly reshaped in characteristic ways, with blur and compression attenuating the GM histogram, and where all the distortions are more greatly separated in the RO and RM histograms.

By examination of Fig. 5, the gradient and relative gradient histograms have a high frequency variation while such variation is ruleless. So the use of a fitting function to those histograms with the least loss is likely to be unproductive. However, following Ruderman [37], who used variance to study the distributions of natural images, we use the histogram variance to characterize the corresponding distributions. Although the variances cannot express all the characters of those histograms, they still represent the most obvious character (viz. the high frequency variation). Given a (normalized to unit sum) histogram $h(x)$, define the variance as

$$Var[h] = \sum_{x} (h(x) - \overline{h})^2, \tag{6}$$

where $\overline{h}$ is the sample mean of the histogram.

Thus we have a 3-dimensional feature vector:

$$Feature = [v_{GM}, v_{RO}, v_{RM}].$$

Denote the variances computed on each of the histograms of the GM, RO, RM maps by v_{GM}, v_{RO} and v_{RM}, respectively.

In order to take into account the multiscale character of natural images, of image distortions, and of visual perception [11,17], we also downsample the image by a factor of 2, then compute the same three features yielding a 6-dimensional feature vector (3 features at each scale). The extracted features are tabulated in Table 1.

5. Learning image quality evaluation

After extracting the gradient features which are ostensibly predictive of image quality in a 6-dimensional space, we build a mapping from image features to image quality via an AdaBoosting BP neural network. The idea of the AdaBoost algorithm is to combine many Weak Learners, the relatively weak learning algorithm which seeks to follow the distribution of the training set [56], while

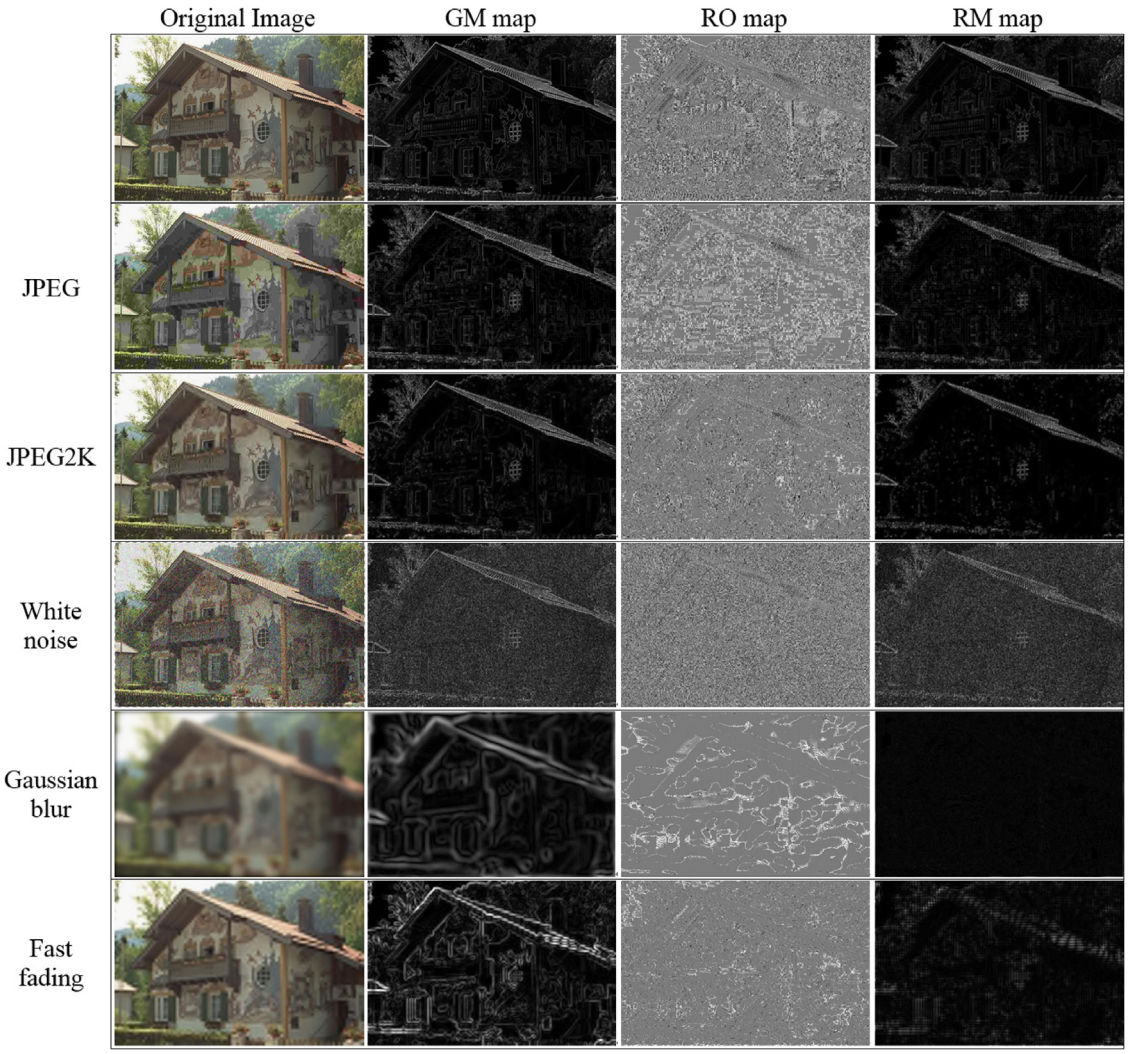

Fig. 4. Gradient and relative gradient maps of a natural undistorted image and five corresponding distorted versions of it.

adaptively adjusting to errors of the weak hypotheses, thereby learning a robust and accurate classifier or regression model [41,57]. Here, the BP neural network is treated as the Weak Learner element of the AdaBoosting algorithm.

A gap between the test and training set may occur when the two sets are from different databases. Using a curve, which is learned from the training set automatically, to normalize the test set is more reasonable than the manual normalization computed with max and min values of training data rigidly. Hence, we design the structure of the BP neural network as two hidden layers, where the first hidden layer auto-normalizes the features by the sigmoid transfer function. Hence, there is no manual normalization of the features. Both hidden layers regress on the image quality. Fig. 6 shows a schematic diagram of the structure of the AdaBoosting BP neural network, where the structure of the BP neural network is described inside the dashed box.

In the BP neural network, the input layer has the same number of neural cells as the dimension of the image features and the output layer is formed by only one neural cell whose output is predictive of the image quality. Both hidden layers contain 6 nodes as does the input layer. The transfer function of the first hidden layer is a tangent sigmoid function whose range is -1 to 1, while that of the second hidden layer is the radial basis function [58].

Given an input (test set X), the overall flow of the Adaboosting BP neural network framework that computes the predicted output on a test set $\hat{Y}$ is described as follows. First, confirm the quantity T of the Weak Learners (viz., the BP neural network) and map the subjective image quality of the training set Y_{train} into the range [0,1] to adjust the transform function of the output layer.

Then, the next few steps need to be done for each Weak Learner. For the *ith* Weak Learner, train it on the training set X_{train} and Y_{train}, and estimate the predicted output of the training set $\hat{Y}^{i}_{train}$ and the test set $\hat{Y}_i$. Consequently, the distribution D_i, which represents the contribution of each training set for computing the training error, of the

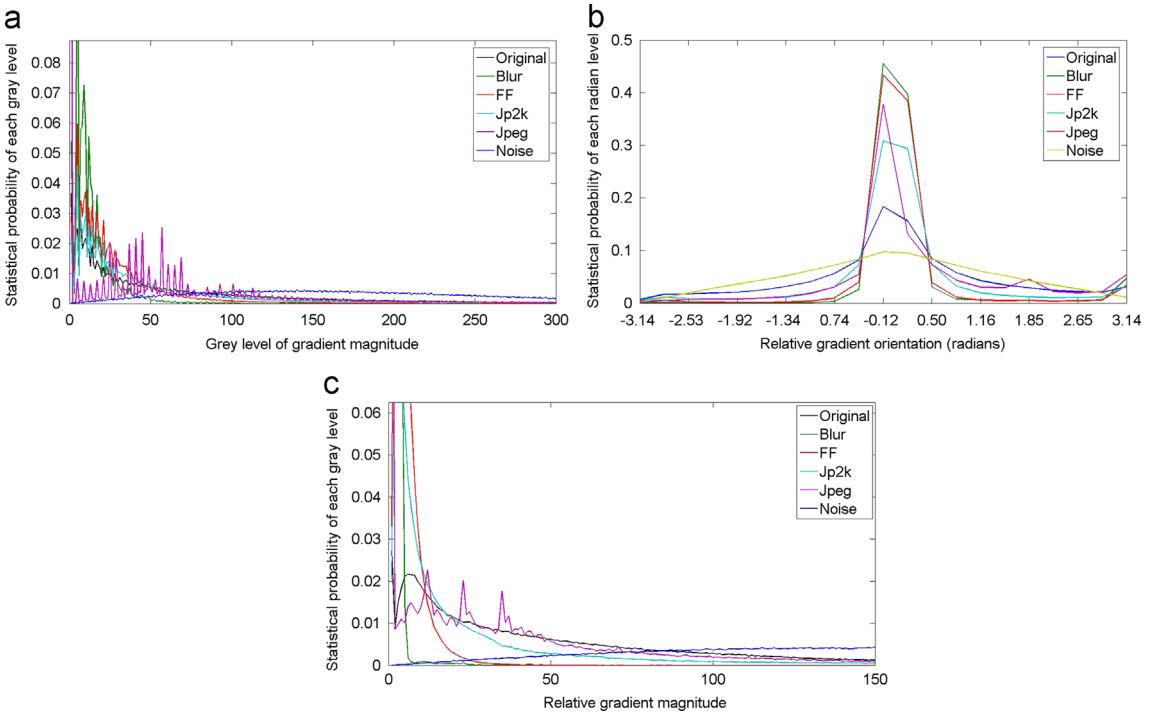

Fig. 5. Histograms of gradient and relative gradient maps of the natural undistorted image in Fig. 4 (top left) and five corresponding distorted versions of it. (a) Gradient magnitude, (b) relative gradient orientation, (c) relative gradient magnitude.

Table 1
Summary of the gradient and relative gradient features.

Feature ID	Feature description
υ_{GM1}, υ_{GM2}	Variances of histogram of gradient magnitude over two scales
υ_{RO1}, υ_{RO2}	Variances of histogram of relative gradient orientation over two scales
υ_{RM1}, υ_{RM2}	Variances of histogram of relative gradient magnitude over two scales

training set X_{train} for the *ith* Weak Learner can be calculated by:

$$D_{i,j} = \begin{cases} 1/K & ,i=1 \\ D_{i-1,j} \times (1+\sigma \cdot l(Y^j_{train} - \hat{Y}^{i-1,j}_{train})) & ,i=2,\ldots,T \end{cases}, \quad (7)$$

where

$$l(x) = \begin{cases} 1, & x > threshold \\ 0, & x \le threshold \end{cases},$$

where K is the number of training vectors in the training set, and j indexes the jth element in a vector whose range is the integers between 1 and K. For example, $D_{i,j}$ stands for the jth element in the vector D_i. The function l is a binary indictor function whose result is 1 when the independent variable in it exceeds the threshold and is 0 otherwise, while the σ is a constant between 0 and 1. For simplicity, we fixed the values of both threshold and σ to 0.1, and $T=10$.

We use an Adaboosting algorithm [59] to measure the evaluation error of the ith Weak Learner Err_i via combining

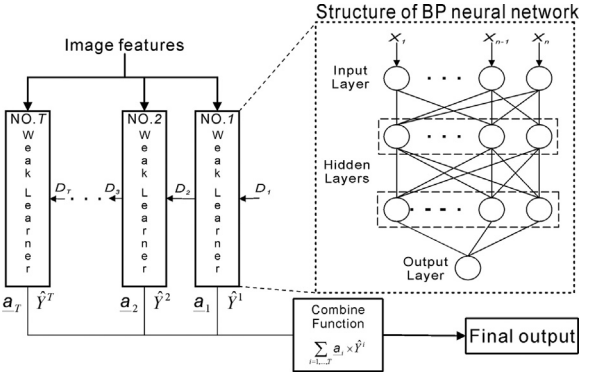

Fig. 6. Structure of the AdaBoosting BP neural network.

the gap between the predicted and real image quality with the corresponding distribution D_i. Hence, the Err_i can be computed using the distribution D_i by

$$Err_i = \sum_{j=1,\ldots,K} D_{i,j} \times l(Y^j_{train} - \hat{Y}^{i,j}_{train}), \quad (8)$$

and utilize a convex function to transform the error of each Weak Learners into its weight, in order to give those Weak Learners with a lower error a higher weight, while the ones with a higher error a smaller weight. The *ith* Weak Learner weight α_i can be defined as

$$\alpha_i = \frac{1}{e^{-b(|Err_i|-c)}}. \quad (9)$$

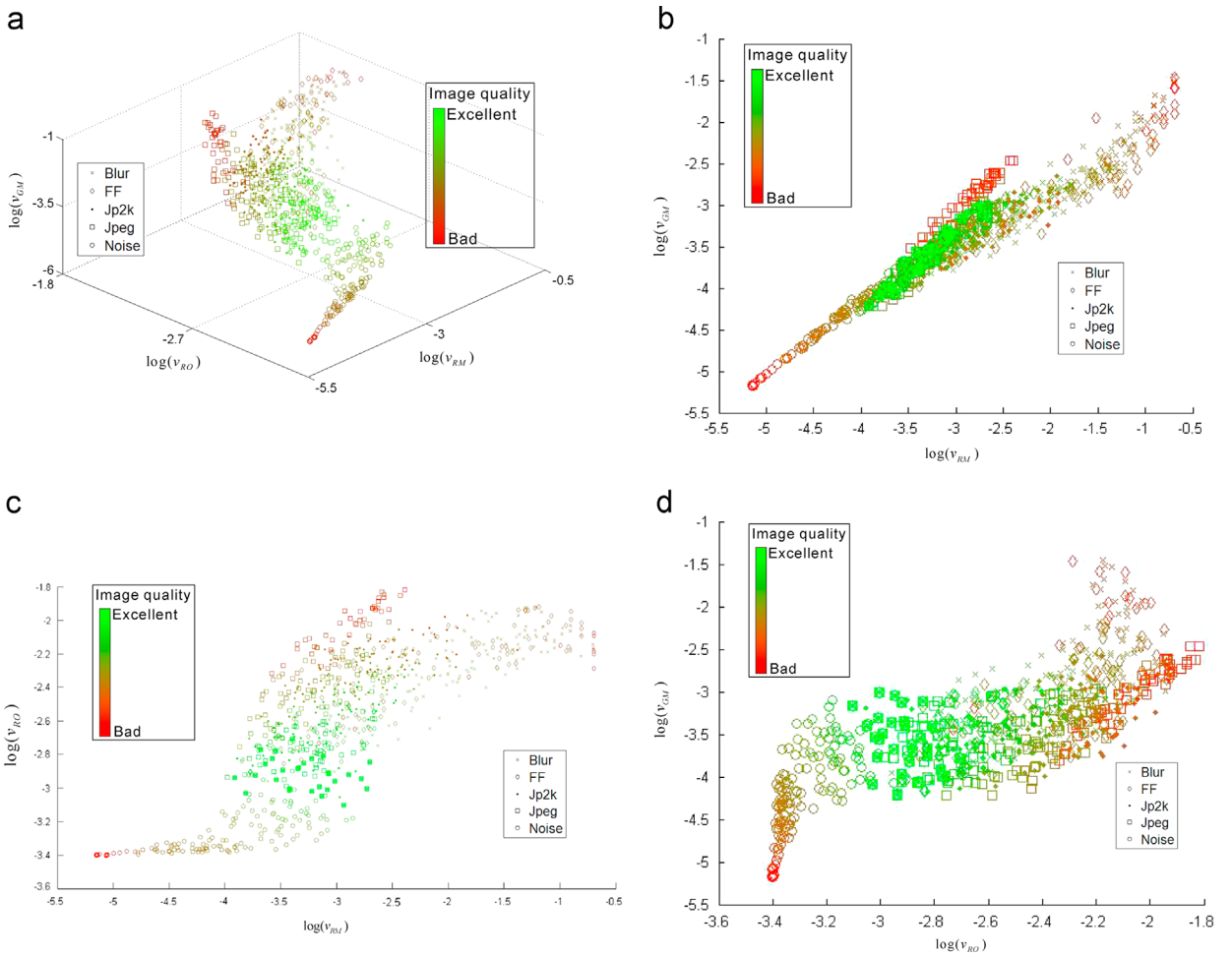

Fig. 7. Scatter plots between each feature group using distortion images drawn from the LIVE IQA database. (a) 3D scatter plots between the variances of GM, RO, RM maps, (b) 2D scatter plots between the variance of RM and GM maps, (c) 2D scatter plots between the variance of RM and RO maps, (d) 2D scatter plots between the variance of GM and RO maps.

Thus, the final output $\hat{Y}$ is a weighted combination of the predicted outputs:

$$\hat{Y} = \sum_{i=1,\ldots,T} \alpha_i \times \hat{Y}^i. \tag{10}$$

6. Experimental results

The overall IQA framework using the features defined here, which we call OG-IQA, was validated on the LIVE IQA database [45,46], which consists of 29 reference images and 779 distorted images disrupted by five distortion categories (JPEG, JPEG2K, white noise, gaussian blur and FF). The features are used to train an AdaBoosting BP neural network engine to conduct distortion classification and quality assessment, respectively. The Spearman's Rank Ordered Correlation Coefficient (SROCC), the linear correlation coefficient (LCC) and the Root Mean Squared Error (RMSE) between the objective quality scores (predicted DMOS) and the subjective quality scores (DMOS) were used as performance evaluation indices. A value close to 1 for SROCC and LCC and a value close to 0 for RMSE indicate superior linear rank-order correlation, and precision with respect to human perception, respectively.

In our experiments, we first evaluated the efficacy of each feature/feature vector used in OG-IQA and compared them and OG-IQA with a set of popular FR and NR approaches. We also study the complexity of OG-IQA and verified the performance of OG-IQA on different IQA databases. In our implementation, we used a random selection of 80% of the images in the LIVE Database as a training set and the remaining (content-separate) 20% as the test set for the AdaBoosting BP neural network and conducted 1000 randomly divided train-test trials. For the compared algorithms, we calculated the quality of the test images predicted by them using the two-step framework [18] except for PSNR, SSIM [2], VIF [3] and BIQA [28].

6.1. Correlation of each feature/feature vector with human opinions

To illustrate the degree by which image quality affects those features, we deployed all the distorted images from

Table 2
Median SROCC of gradient and relative gradient features.

SROCC	JP2k	JPEG	NOISE	BLUR	FF	ALL
ν_{GM1}, ν_{GM2}	0.5223	0.6780	0.9649	0.9519	0.6797	0.6823
ν_{RO1}, ν_{RO2}	0.9462	0.9633	0.9617	0.9541	0.8632	0.9223
ν_{RM1}, ν_{RM2}	0.7769	0.6987	0.9666	0.9252	0.7587	0.7443

Table 3
Median LCC of gradient and relative gradient features.

LCC	JP2k	JPEG	NOISE	BLUR	FF	ALL
ν_{GM1}, ν_{GM2}	0.6021	0.8077	0.9755	0.9515	0.7806	0.7421
ν_{RO1}, ν_{RO2}	0.9546	0.9757	0.9701	0.9566	0.8805	0.9193
ν_{RM1}, ν_{RM2}	0.8088	0.7586	0.9739	0.9467	0.8204	0.7617

Table 4
Median RMSE of gradient and relative gradient features.

RMSE	JP2k	JPEG	NOISE	BLUR	FF	ALL
ν_{GM1}, ν_{GM2}	22.9053	20.6923	7.3328	7.3572	19.2799	20.9879
ν_{RO1}, ν_{RO2}	8.5049	7.6549	8.0485	6.9552	14.5817	12.2597
ν_{RM1}, ν_{RM2}	16.9782	22.9655	7.5615	7.7256	17.5331	20.2969

Table 5
Median SROCC on the LIVE IQA database.

SROCC	JP2K	JPEG	NOISE	BLUR	FF	ALL
PSNR	0.9041	0.8946	0.9829	0.8073	0.8941	0.8834
SSIM	0.9609	0.9737	0.9702	0.9515	0.9560	0.9484
VIF	0.9682	0.9820	0.9844	0.9715	0.9626	0.9633
BIQI	0.8587	0.7171	0.9748	0.9171	0.7681	0.7657
CBIQ	0.9130	0.9638	0.9581	0.9203	0.8832	0.8965
DIIVINE	0.9430	0.9086	0.9839	0.9567	0.8948	0.9254
BLIINDS-II	0.9478	0.9575	0.9634	0.9350	0.9018	0.9326
BRISQUE	0.9327	0.9341	0.9890	0.9505	0.8756	0.9398
BIQA	0.9535	0.9570	0.9884	0.9609	0.9379	0.9509
OG-IQA	0.9370	0.9643	0.9867	0.9612	0.8985	0.9500

Table 6
Median LCC on the LIVE IQA database.

LCC	JP2K	JPEG	NOISE	BLUR	FF	ALL
PSNR	0.8859	0.8780	0.9829	0.8036	0.8926	0.8642
SSIM	0.9710	0.9819	0.9863	0.9556	0.9622	0.9463
VIF	0.9809	0.9891	0.9921	0.9771	0.9686	0.9616
BIQI	0.8742	0.7241	0.9810	0.9171	0.8272	0.7771
CBIQ	0.9102	0.9438	0.9410	0.9403	0.8991	0.8951
DIIVINE	0.9497	0.9316	0.9883	0.9451	0.9198	0.9275
BLIINDS-II	0.9614	0.9733	0.9735	0.9422	0.9247	0.9422
BRISQUE	0.9377	0.9717	0.9934	0.9487	0.9049	0.9467
BIQA	0.9620	0.9835	0.9920	0.9664	0.9451	0.9587
OG-IQA	0.9459	0.9827	0.9904	0.9673	0.9110	0.9524

the LIVE IQA database [45,46] covering a wide range of human opinion scores, and plotted their feature vectors in Fig. 7. Each point represents an image and can be distinguished by its shape and color (from green to red, where green indicates very high image quality while red represents very low image quality). We can observe that the image features begin to occur at the ends of the plotting as the image quality degrades. At the low image quality level, the white noise and JPEG distorted image features can be well separated, whereas the JP2k, BLUR and the fast fading distorted image features overlap together, because that all three distortion are mainly degrade image via blurring.

We also validate the performances of each feature vector in Tables 2–4. It may be seen that each feature is in agreement with human subjective opinion in varying degrees according to distortion and contributes to algorithm performance in different ways. Furthermore, we can observe that the features from RO map are more effective than others for JPEG and JP2k distortions. Since JPEG and JP2k mainly contain the blocking, the blur and ringing, respectively, they will degrade the image quality in local regions. Hence, both distortions can affect the gradient orientation much more seriously than the gradient magnitude due to the limitations detailed in Section 3.

6.2. Statistical performance comparison against state-of-the-art

In order to validate the statistical performance of OG-IQA, we compared it against three FR approaches (PSNR, SSIM [2] and VIF [3]) and six NR approaches (DIIVINE [16], BLIINDS-II [17], BIQI [18], CBIQ [33], BRISQUE [19] and BIQA [28]). All the models were trained separately on each of the five different distortion types, and also on all five types. All three indexes were obtained using the same 80% training-20% testing protocol over 1000 iterations, with the results listed in Tables 5–7. To further test the effectiveness of our algorithm, we also determined its performance on the TID2013 database [60] and the LIVEMD database [61], as shown in Fig. 8 and Table 8. The TID2013 database consists of 25 reference images and 3000 distorted images over 24 distortion categories, while the LIVEMD database has 15 reference images and 450 multiply distorted images, including blur followed by JPEG (BJ) and blur followed by noise (BN). For TID2013 database, we tested OG-IQA only on the 24 natural reference images and associated 19 distortion categories, except for the 5 color distortion categories.

From the experimental results on the LIVE IQA database, it may be observed that OG-IQA correlates well with human subjective opinions of image quality and achieves highly competitive performance against existing NR IQA models (indeed, it is only slightly inferior to the top-performing FR IQA model VIF and the NR IQA approach BIQA). The results on the TID2013 and LIVEMD databases (see Fig. 8 and Table 8) also show that OG-IQA performs well across a wide variety of distortions. It is worth noting that OG-IQA only requires the generation of an efficient 6-dimensional feature vector, while the feature dimensions

Table 7
Median RMSE on the LIVE IQA database.

RMSE	JP2K	JPEG	NOISE	BLUR	FF	ALL
PSNR	11.7312	15.3627	5.4190	11.0876	12.8265	13.7388
SSIM	6.0037	5.9826	4.6378	5.3804	7.6237	8.8403
VIF	4.9039	4.6802	3.5170	3.8891	6.9530	7.5035
BIQI	13.9383	24.3130	6.4001	9.5840	17.4349	19.6292
CBIQ	9.0130	18.6518	0.5231	8.6302	13.6837	12.7917
DIIVINE	9.0021	12.7674	5.0479	7.8777	12.1846	11.6621
BLIINDS-II	7.8225	8.0873	7.5637	8.0368	11.8464	10.4938
BRISQUE	9.9458	8.2839	3.7676	7.6569	13.2282	10.0548
BIQA	8.4471	6.7571	4.4512	6.6180	10.8117	9.2097
OG-IQA	9.2754	6.5073	4.5628	6.0938	12.7999	9.5267

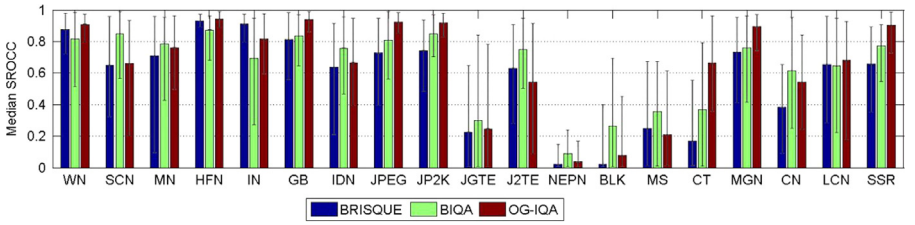

Fig. 8. SROCC distributions on the TID2013 database. The histogram shows the median SROCC values of each algorithm while the line in each column means its range of the mild outliers.

Table 8
The performance on the LIVE MD IQA database.

		PSNR	SSIM	BRISQUE	BIQA	OG-IQA
SROCC	BJ	0.7636	0.8912	0.8901	0.8680	0.8765
	BN	0.7781	0.9097	0.8851	0.6812	0.8536
LCC	BJ	0.8007	0.8500	0.9286	0.9137	0.9244
	BN	0.8060	0.8713	0.9024	0.7057	0.9016
RMSE	BJ	23.4543	10.0778	7.7702	13.1277	7.2592
	BN	23.1530	8.9742	6.8885	7.7607	7.8300

of BIQI, DIIVINE, BLIINDS-II, BRISQUE and BIQA are 18, 88, 24, 36 and 40, respectively.

6.3. Statistical significance and hypothesis testing

Fig. 9 shows box plots of the SROCC distribution of each algorithm over 1000 trials. Although there exist differences in the median correlations between the different algorithms (see Tables 5–7), these differences may not be statistically relevant. Hence, to evaluate the statistical significance of the performance of the algorithms considered, we conducted the multiple comparisons test [62] using the SROCC values obtained from the 1000 train-test trials, and tabulated the results in Table 9. The numbers in first row indicate that the minus of the mean value of each group, and a 95% confidence interval for the mean is listed in second and third rows, respectively. For example, the numbers in column BRISQUE, indicate that the SROCC values mean of our method minus the mean of BRISQUE is estimated to be 0.012, while the difference of the means with a 95% confidence interval is [0.0081–0.0159].

From Table 9 we may conclude that OG-IQA is competitive with the popular IQA approaches such as PSNR, SSIM, BIQI, DIIVINE, BLIINDS-II, and top-performing NR approaches such as BRISQUE and BIQA. The stability of OG-IQA matches that of BIQA as observed from Fig. 9. This performance summary suggests that OG-IQA is an attractive option for NR assessment of picture quality.

6.4. Variation with window size

From Table 10, it may be observed that the algorithm performance varies with the size of the window over which the gradient quantities are computed.

The performance is marginally better with decreased window size, likely since the computed features are more sensitive to highly local distortions.

6.5. Statistical performance comparison against different regressors

In order to validate the effectiveness of the regressor used in our method, we use our image features to compare against other two regressors, and the results are listed in Table 11.

The results show that the regressors based on neural network have a better performance than the one based on SVR, while the AdaBoosting neural network has the best performance in almost all contrast items. We may speculate that the features from RO, RM and GM may have different importance for evaluating the image quality and those features may be recombined via linear combination to improve their robustness.

6.6. Database independence

To prove the database independence of OG-IQA, we also tested it on the TID2013 image database, using the 24

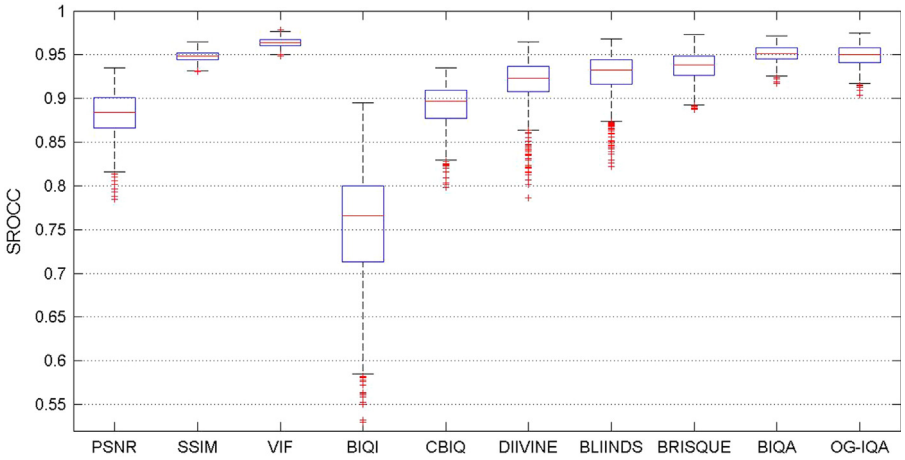

Fig. 9. Box plots of SROCC distributions of IQA models on the LIVE IQA database. The red line in the rectangle means the median values of the 1000 trials SROCC values for each algorithm, while the upper and lower ends of the rectangle means the first and third quartiles, respectively. The length of the dotted line means the range of the mild outliers, and the symbol "+" represents the extreme outliers for each algorithm.

Table 9
Multiple comparisons test on SROCC of each IQA algorithm.

	PSNR	SSIM	VIF	BIQI	CBIQ	DIIVINE	BLIINDS-II	BRISQUE	BIQA
Mean	0.0668	0.0008	−0.0145	0.1966	0.0575	0.0298	0.0217	0.0120	−0.0017
Upper mean	0.0629	0.0031	−0.0184	0.1927	0.0535	0.0258	0.0178	0.0081	−0.0056
Lower mean	0.0707	0.0047	−0.0106	0.2005	0.0614	0.0337	0.0256	0.0159	0.0023

Table 10
Median SROCC of OG-IQA on the LIVE IQA database with different window sizes.

M, N	JP2K	JPEG	NOISE	BLUR	FF	ALL
4, 4	0.9347	0.9573	0.9822	0.9667	0.9002	0.9381
5, 5	0.9313	0.9544	0.9775	0.9639	0.8905	0.9327
6, 6	0.9208	0.9476	0.9738	0.9569	0.8660	0.9194
9, 9	0.8964	0.9165	0.9689	0.9416	0.8592	0.8844
12, 12	0.8468	0.8859	0.9668	0.9377	0.7641	0.8531

Table 11
Median SROCC of OG-IQA features using different regressors on the LIVE IQA database.

	JP2K	JPEG	NOISE	BLUR	FF	ALL
Our method	0.9370	0.9643	0.9867	0.9612	0.8985	0.9500
SVR	0.9522	0.9672	0.9812	0.9518	0.8669	0.9265
BP Neural Network	0.9395	0.9594	0.9823	0.9609	0.8848	0.9384

Table 12
Median SROCC of OG-IQA on the TID2013 database.

	JP2K	JPEG	NOISE	BLUR	ALL
PSNR	0.8904	0.9150	0.9420	0.9661	0.9216
SSIM	0.9489	0.9316	0.8742	0.9704	0.9212
BRISQUE	0.8961	0.8585	0.9000	0.8709	0.8819
BIQA	0.9421	0.8930	0.8128	0.8819	0.8922
OG-IQA$_{manual}$	0.8906	0.8835	0.8606	0.8827	0.8821
OG-IQA$_{auto}$	0.8919	0.8861	0.8705	0.8923	0.8946

Table 13
Median SROCC of OG-IQA on the LIVE IQA database.

	JP2K	JPEG	NOISE	BLUR	ALL
PSNR	0.9041	0.8946	0.9829	0.8073	0.8834
SSIM	0.9609	0.9737	0.9702	0.9515	0.9484
BRISQUE	0.8998	0.9119	0.9659	0.9094	0.9151
BIQA	0.8668	0.9204	0.9674	0.9371	0.9191
OG-IQA$_{manual}$	0.8719	0.9136	0.9774	0.9187	0.9161
OG-IQA$_{auto}$	0.8976	0.9262	0.9778	0.9201	0.9250

Table 14
Classification accuracy with 1000 train-test trials.

	JP2K	JPEG	NOISE	BLUR	FF	ALL
Accuracy (%)	81.08	79.45	100	92	24	75.47

natural reference images and the same four commonly occurring distortion categories: JPEG2000, JPEG, Gaussian noise, and Gaussian blur in it.

We trained OG-IQA on the LIVE IQA Database to obtain a model which we then tested on the TID2013 Database. In other words, we used the images in the LIVE IQA database as a training set and the images from TID2013 Database as the test set. For further comparison, we also trained our model on the TID2013 database and tested it on the LIVE IQA database. For OG-IQA, we verify the effectiveness of the auto-normalization process and manual normalization process in our method. The median SROCC was again used as the performance index, and is tabulated in Tables 12

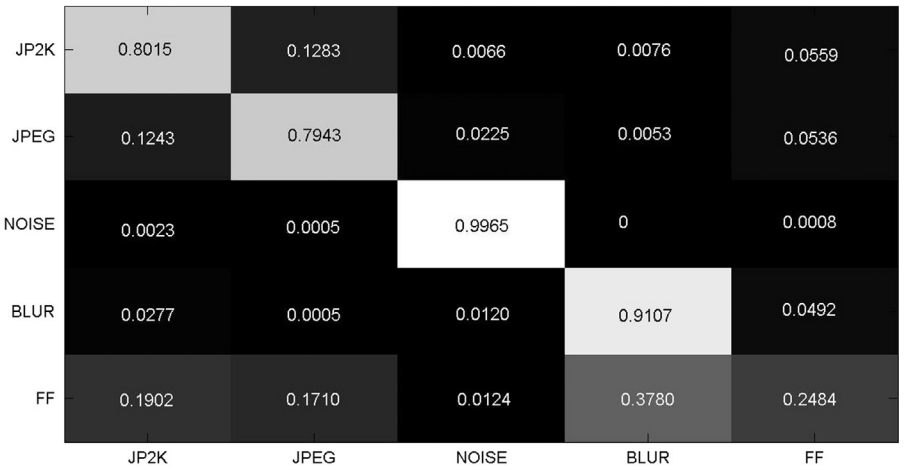

Fig. 10. Mean confusion matrix for distortion classifier across 1000 train-test trials.

Table 15
Comparison of time complexity (time for feature extraction) of five NR IQA algorithms.

	The algorithm complexity	The run time (s)
DIIVINE(88D)	$O(K(\log(K)+d+K))$	30.5294
BLIINDS-II(24D)	$O((K/(d^2))^*\log(K/(d^2)))$	133.5213
BRISQUE(36D)	$O(K^*d^2)$	0.1340
BIQA(40D)	$O(K^*(d_1+d_2))$	0.1140
OG-IQA(6D)	$O(K^*d)$	0.1060

Table 16
Comparison of time complexity (time for training) of three regressor methods.

	The algorithm complexity	The run time (s)
Our method	$T^*(I^*L^*C+C^*L)$	8.3930
BP neural network	I^*L^*C	1.9660
SVR	D^*L^2	0.0930

and 13. It may be observed that OG-IQA trained in this way achieved highly competitive performance on both the LIVE and the TID2013 Databases.

6.7. Classification accuracy

We analyzed the classification performance of our algorithm on the LIVE IQA database. The input of the neural network is also the six image features, but the output is a 5-dimensional vector of predicted distortion type. For example, the output labeling for JP2K distortion is the vector [1,0,0,0,0] while the vector indicating JPEG is [0,1,0,0,0]. The performance indicator is the median classification accuracy on each distortion category as well as across all distortion categories over the 1000 trials. These results are shown in Table 14. We also show the confusion matrix for each category of distortion in Fig. 10. The vertical axis of the confusion matrix represents the true distortion class while the horizontal axis denotes the predicted distortion class. The numerical values are the confusion probabilities obtained over 1000 trials.

From Table 14, we can observe that the FF distortion is the least distinguishable distortion, while the others are highly distinguishable. However, the absolute classification accuracy is not of importance to the predicted performance of our method, because what relative to the performance is not an absolute classification, but an indication of the amount of each distortion present in the image [18].

Fig. 10 shows that the FF distortion is mainly misclassified as JP2k and blur. This is cause that the FF distortion images are multidistorted by a JP2k compressed and a processing simulating packet loss and exhibits blur and ringing.

6.8. Computational complexity

Since the computation time of NR IQA models is mainly consumed in the process of feature extraction, we compared the efficiency of feature extraction against that of four other holistic no-reference approaches (DIIVINE [16], BLIINDS-II [17], BRISQUE [19] and BIQA [28]) assuming the input image is $K=512\times768$ pixels. Let d be the window size (in pixels) used for feature computation. For example, d in DIIVINE is the neighborhood vector size, while d_1 and d_2 in BIQA are the spans of the gradient operators (i.e., the Laplacian of Gaussian and the directional derivative operators) and the size of the joint probability matrix respectively, and d in OG-IQA is the size of the gradient operators (i.e., the local neighborhood used to compute the directional derivative operators). The results in Table 15 show that OG-IQA is faster than DIIVINE, BLIINDS-II, BRISQUE, and BIQA, using a Dell desktop computer with a quad-core CPU, 3.4 GHz and 4 GB RAM.

Furthermore, we also analyze the training and the prediction complexity using other two regressors (viz. SVR and BP neural network) with our 6-dimension features on the LIVE database. Let D be the dimension of the features, L be the size of the training set and the test set and I be the max iteration set in the neural network based algorithms. For AdaBoosting algorithm, the T represents the number of

Table 17
Comparison of time complexity (time for test) of three regressor methods.

	The algorithm complexity	The run time (s)
Our method	T^*L^*C	0.4990
BP neural network	L^*C	0.0940
SVR	D^*L	0.0160

the Weak Learners and the C means the number of link between each neuron. The results (see Tables 16 and 17) show that the Running Time of the SVR is much faster than that of the neural network. However, we can assume that the neural network based methods can deal with the big data more faster than the SVR in time complexity, because the time complexity of SVR is based on the quadratic of the training set, and the neural network based methods can be optimized via parallel processing.

7. Conclusion

We presented OG-IQA, a novel NR IQA model that uses efficient perceptual image features and an advanced feature learning algorithm. The performance of OG-IQA validates the use of features descriptive of image structure that use the image relative gradient orientation as a complementary and effective 'quality-aware' source of information for conducting NR IQA. Indeed, the experimental results show that OG-IQA is highly competitive with the most popular IQA approaches, and has a very low time complexity.

Going forward, we believe that the concept of relative gradient values (computed in space–time) may prove useful for the development of blind video quality models, an area that remains open. It is also possible that the ideas herein could be improved by incorporating measures of image content, as in the FR IQA model described in [63].

References

[1] A.K. Moorthy, A. Mittal, A.C. Bovik, Perceptually optimized blind repair of natural images, Signal Process. Image Commun. 28 (10) (2013) 1478–1493.
[2] Z. Wang, A.C. Bovik, H.R. Sheikh, E.P. Simoncell, Image quality assessment: from error visibility to structural similarity, IEEE Trans. Image Process. 13 (4) (2004) 600–612.
[3] H.R. Sheikh, A.C. Bovik, Image information and visual quality, IEEE Trans. Image Process. 15 (2) (2006) 430–444.
[4] L. Zhang, X. Mou, D. Zhang, FSIM: a feature similarity index for image quality assessment, IEEE Trans. Image Process. 20 (8) (2011) 2378–2386.
[5] X. Zhang, X. Feng, W. Wang, W. Xue, Edge strength similarity for image quality assessment, IEEE Signal Process. Lett. 20 (4) (2013) 319–322.
[6] W. Xue, L. Zhang, X. Mou, A.C. Bovik, Gradient magnitude similarity deviation: a highly efficient perceptual image quality index, IEEE Trans. Image Process. 23 (2) (2013) 684–695.
[7] A. Liu, W. Lin, M. Narwaria, Image quality assessment based on gradient similarity, IEEE Trans. Image Process. 21 (4) (2012) 1500–1512.
[8] J. Zhu, N. Wang., Image quality assessment by visual gradient similarity, IEEE Trans. Image Process. 21 (3) (2012) 919–933.
[9] Y. Yang, D. Tu, G. Cheng, Image quality assessment using histograms of oriented gradients, in: Proceedings of International Conference on Intelligent Control and Information Processing, 2013, pp. 555–559.
[10] H. Zhang, Y. Huang, X. Chen, D. Deng, MLSIM: a multi-level similarity index for image quality assessment, Signal Process. Image Commun. 28 (10) (2013) 1464–1477.
[11] Z. Wang, E. P. Simoncelli, A. C. Bovik, Multiscale structural similarity for image quality assessment, in: Proceedings of Asilomar Conference on Signals, Systems & Computers, Vol. 2, 9–12 Nov. 2003, Pacific Grove, CA, USA, 2003, pp. 1398–1402.
[12] Y. Wang, T. Jiang, M. Siwei and W. Gao, Image quality assessment based on local orientation distributions, in: Proceedings of the 28th Picture Coding Symposium (PCS), 8–10 Dec. 2010, Nagoya, Japan, 2010, pp. 274–277.
[13] B. P. Bondzulic and V. S. Petrovic, Edge based objective evaluation of image quality, in: Proceedings of the 18th IEEE International Conference on Image Processing (ICIP), 11–14 Sep. 2011, Brussels, Piscataway, NJ, USA, 2011 pp. 3305–3308.
[14] K. Gu, G. Zhai, W. Lin, X. Yang and W. Zhang, An efficient color image quality metric with local-tuned-global model, in: Proceedings of IEEE International Conference on Image Processing (ICIP 2014), 27–30 Jan. 2015, Paris, France, pp. 506–510.
[15] G. Cheng, J. Huang, Z. Liu, L. Cheng, Image quality assessment using natural image statistics in gradient domain, AEU-Int. J. Electron. Commun. 65 (5) (2011) 392–397.
[16] A.K. Moorthy, A.C. Bovik, Blind image quality assessment: from natural scene statistics to perceptual quality, IEEE Trans. Image Process. 20 (12) (2011) 3350–3364.
[17] M.A. Saad, A.C. Bovik, C. Charrier, Blind image quality assessment: a natural scene statistics approach in the DCT domain, IEEE Trans. Image Process. 21 (8) (2012) 3339–3352.
[18] A.K. Moorthy, A.C. Bovik, A two-step framework for constructing blind image quality indices, IEEE Signal Process. Lett. 17 (5) (2010) 513–516.
[19] A. Mittal, A.K. Moorthy, A.C. Bovik, No-reference image quality assessment in the spatial domain, IEEE Trans. Image Process. 21 (12) (2012) 4695–4708.
[20] M.J. Chen, A.C. Bovik, No-reference image blur assessment using multiscale gradient, EURASIP J. Image Video Process. 2011 (1) (2011) 1–11.
[21] T. Brandao, M.P. Queluz, No-reference image quality assessment based on DCT-domain statistics, Signal Process. 88 (4) (2008) 822–833.
[22] H.R. Sheikh, A.C. Bovik, L. Cormack, No-reference quality assessment using natural scene statistics: JPEG2000, IEEE Trans. Image Process. 14 (11) (2005) 1918–1927.
[23] C. Li, A.C. Bovik, X. Wu, Blind image quality assessment using a general regression neural network, IEEE Trans. Neural Netw. 22 (5) (2011) 793–799.
[24] M.A. Saad, A.C. Bovik, C. Charrier, A DCT statistics-based blind image quality index, IEEE Signal Process. Lett. 17 (6) (2010) 583–586.
[25] S. Gabarda, G. Cristobal, Blind image quality assessment through anisotropy, J. Opt. Soc. A. (Optics, Image Science and Vision) 24 (12) (2007) B42–B51.
[26] X. Gao, F. Gao, D. Tao, X. Li, Universal blind image quality assessment metrics via natural scene statistics and multiple kernel learning, IEEE Trans. Neural Netw. Learn. Syst. 24 (12) (2013) 2013–2026.
[27] L. Liu, H. Dong, H. Huang, A.C. Bovik, No-reference image quality assessment in curvelet domain, Signal Process. Image Commun. 29 (4) (2014) 494–505.
[28] W. Xue, X. Mou, L. Zhang, A.C. Bovik, X. Feng, Blind image quality assessment using joint statistics of gradient magnitude and laplacian features, IEEE Trans. Image Process. 23 (11) (2014) 4850–4862.
[29] W. Hou, X. Gao, D. Tao, X. Li, Blind image quality assessment via deep learning, IEEE Trans. Neural Netw. Learn. Syst. 26 (6) (2014) 1275–1286.
[30] M. Narwaria, W. Lin, Objective image quality assessment based on support vector regression, IEEE Trans. Neural Netw. 21 (3) (2010) 515–519.
[31] A. Mittal, G.S. Muralidhar, J. Ghosh, A.C. Bovik, Blind image quality assessment without human training using latent quality factors, IEEE Signal Process. Lett. 19 (2) (2012) 75–78.
[32] W. Xue, L. Zhang, X. Mou, Learning without human scores for blind image quality assessment, in: Proceedings of IEEE Conference on Computer Vision and Pattern Recognition (CVPR 2013), 23–28 June 2013, Portland, OR, USA.
[33] P. Ye, D. Doermann, No reference image quality assessment using visual codebooks, IEEE Trans. Image Process. 21 (7) (2012) 3129–3138.

[34] P. Ye, J. Kumar, L. Kang, and D. Doermann, Unsupervised feature learning framework for no reference image quality assessment, in: Proceedings of IEEE Computer Society Conference on Computer Vision and Pattern Recognition (CVPR 2012), 16–21 June 2012, Los Alamitos, CA, USA, pp. 1098–1105.
[35] K. Gu, G. Zhai, X. Yang, W. Zhang, Using free energy principle for blind image quality assessment, IEEE Trans. Multimed. 17 (1) (2015) 50–63.
[36] K. Gu, G. Zhai, W. Lin, X. Yang, W. Zhang, No-reference image sharpness assessment in autoregressive parameter space, IEEE Trans. Image Process. 24 (10) (2015) 3218–3231.
[37] D.L. Ruderman, The statistics of natural images, Netw. Comput. Neural Syst. 5 (4) (1994) 517–548.
[38] N. Dalal, B. Triggs, Histograms of oriented gradients for human detection, in: Proceedings of IEEE Computer Society Conference on Computer Vision and Pattern Recognition (CVPR 2005), vol. 1, 20–25 June 2005, San Diego, CA, USA, pp. 886–893.
[39] C. -C. Su, A.C. Bovik, Closed-form correlation model of oriented bandpass natural images, IEEE Signal Process. Lett. 22 (1) (2015) 21–25.
[40] L.K. Hansen, P. Salamon, Neural network ensembles, IEEE Trans. Pattern Anal. Mach. Intell. 12 (10) (1990) 993–1001.
[41] Y. Freund, R. E. Schapire, A desicion-theoretic generalization of on-line learning and an application to boosting, in: Proceedings of the Second European Conference on Computational Learning Theory, *Lecture Notes in Computer Science*, vol. 904, 1995, pp. 23–37.
[42] P.L. Bartlett, M. Traskin, Adaboost is consistent, Adv. neural inf. proces. syst. 8 (2007) 2347–2368.
[43] D. W. Opitz, R. F. Maclin, An empirical evaluation of bagging and boosting for artificial neural networks, in: Proceedings of International Conference on Neural Networks vol. 3, 9–12 Jun. 1997, pp. 1401–1405.
[44] B.P. Roe, H.J. Yang, J. Zhu, Y. Liu, I. Stancu, G. McGregor, Boosted decision trees as an alternative to artificial neural networks for particle identification, Nucl. Instrum. Methods Phys. Res. A Accel. Spectrom. Detect. Assoc. Equip. 543 (2) (2005) 577–584.
[45] H. R. Sheikh, Z. Wang, L. Cormack and A. C. Bovik, LIVE Image Quality Assessment Database Release 2, ⟨http://live.ece.utexas.edu/research/quality⟩.
[46] H.R. Sheikh, M.F. Sabir, A.C. Bovik, A statistical evaluation of recent full reference image quality assessment algorithms, IEEE Trans. Image Process. 15 (11) (2006) 3440–3451.
[47] D.J. Field, Relations between the statistics of natural images and the response properties of cortical cells, J. Opt. Soc. Am. A, Opt. Image Sci. 4 (12) (1987) 2379–2394.
[48] A. Mittal, R. Soundararajan, A.C. Bovik, Making a 'completely blind' image quality analyzer, IEEE Signal Process. Lett. 20 (3) (2013) 209–212.
[49] A.C. Bovik, Automatic prediction of perceptual image and video quality, Proc. IEEE 101 (9) (2013) 2008–2029.
[50] D.H. Hubel, T.N. Wiesel, Receptive fields, binocular interaction and functional architecture in the cat's visual cortex, J. Physiol. 160 (1) (1962) 106–154.
[51] M. Clark, A.C. Bovik, Experiments in segmenting texton patterns using localized spatial filters, Pattern Recognit. 22 (6) (1989) 707–717.
[52] D.G. Lowe, Distinctive image features from scale-invariant keypoints, Int. J. Comput. Vis. 60 (2) (2004) 91–110.
[53] K. Velmurugan, S.S. Baboo, Image retrieval using harris corners and histogram of oriented gradients, Int. J. Comput. Appl. 24 (7) (2011) 6–10.
[54] P.J. Burt, E.H. Adelson, The Laplacian pyramid as a compact image code, IEEE Trans. Commun. 31 (4) (1983) 532–540.
[55] E. P. Simoncelli, W. T. Freeman, The steerable pyramid: a flexible architecture for multi-scale derivative computation, in: Proceedings of the IEEE Computer Society International Conference on Image Processing, vol. 3, 1995, pp. 3444–3444.
[56] M. Korytkowski, L. Rutkowski, R. Scherer, On combining backpropagation with boosting, in: Proceedings of IEEE International Joint Conference on Neural Networks, 2006, pp. 1274–1277.
[57] V. Gomez-Verdejo, J. Arenas-Garcia, A.R. Figueiras-Vidal, A dynamically adjusted mixed emphasis method for building boosting ensembles, IEEE Trans. Neural Netw. 19 (1) (2008) 3–17.
[58] K.M. Tao, A closer look at the radial basis function (RBF) networks, in: Proceedings of Asilomar Conference on Signals, Systems & Computers, vol. 1, 1–3 Nov. 1993, pp. 401–405.
[59] D. P. Solomatine, D. L. Shrestha, AdaBoost. RT: a boosting algorithm for regression problems, in: Proceedings of IEEE International Joint Conference on Neural Networks, vol. 2, 25–29 July 2004, pp. 1163–1168.
[60] N. Ponomarenko, O. Ieremeiev, V. Lukin, K. Egiazarian, L. Jin, J. Astola, B. Vozel, K. Chehdi, M. Carli, F. Battisti, C.-C. J. Kuo, Color image database.
[61] Dinesh Jayaraman, Anish Mittal, Anush K. Moorthy, Alan C. Bovik, Objective image quality assessment of multiply distorted images, in: Proceedings of Conference Record of the 46th Asilomar Conference on Signals, System and Computers (ASILOMAR), 2012, pp. 1693–1697.
[62] Y. Hochberg, A.C. Tamhane, Multiple Comparison Procedures, Wiley, New York, 1987.
[63] C. Li, A.C. Bovik, Content-partitioned structured similarity index for image quality assessment, Signal Process. Image Commun. 25 (7) (2010) 519–526.